Effects of aquifer geometry on seawater intrusion in annulus segment island aquifers

Zhaoyang Luo[1,2], Jun Kong[1,3,#], Chengji Shen[1], Pei Xin[1], Chunhui Lu[1], Ling Li[4],

David Andrew Barry[2]

[1]State Key Laboratory of Hydrology-Water Resources and Hydraulic Engineering, Hohai

University, Nanjing, China

[2]Ecological Engineering Laboratory (ECOL), Environmental Engineering Institute (IIE),

Faculty of Architecture, Civil and Environmental Engineering (ENAC), École Polytechnique

Fédérale de Lausanne (EPFL), Lausanne, Switzerland

[3]Jiangsu Key Laboratory of Coast Ocean Resources Development and Environment Security,

Hohai University, Nanjing, China

[4]School of Engineering, Westlake University, Hangzhou, China

[#]Corresponding author: Jun Kong (kongjun999@126.com)

Resubmitted to *Hydrology and Earth System Sciences* on 8 November 2021

Abstract

Seawater intrusion in island aquifers was considered analytically, specifically for annulus segment aquifers (ASAs), i.e., aquifers that (in plan) have the shape of an annulus segment. Based on the Ghijben-Herzberg and hillslope-storage Boussinesq equations, analytical solutions were derived for steady-state seawater intrusion in ASAs, with a focus on the freshwater-seawater interface and its corresponding watertable elevation. Predictions of the analytical solutions compared well with experimental data, and so they were employed to investigate the effects of aquifer geometry on seawater intrusion in island aquifers. Three different ASA geometries were compared: convergent (smaller side facing the lagoon), rectangular and divergent (larger side facing the sea). Depending on the aquifer geometry, seawater intrusion was found to vary greatly, such that the assumption of a rectangular aquifer to model an ASA can lead to poor estimates of seawater intrusion. Other factors being equal, compared with rectangular aquifers, seawater intrusion is more extensive and watertable elevation is lower in divergent aquifers, with the opposite tendency in convergent aquifers. Sensitivity analysis further indicated that the effects of aquifer geometry on seawater intrusion and watertable elevation vary with aquifer width and distance from the circle center to the inner arc (the lagoon boundary for convergent aquifers while the internal no-flow boundary for divergent aquifers). A larger aquifer width and distance from the circle center to the inner arc weaken the effects of aquifer geometry and hence differences in predictions for the three geometries become less pronounced.

Keywords: sharp-interface; steady-state analytical solution; atoll aquifer; annulus segment aquifer, seawater intrusion

Key Points

➤ Analytical solutions of steady-state seawater intrusion were derived for annulus segment aquifers

➤ Among three different aquifer geometries, divergent aquifers have the lowest watertable and hence the most extensive seawater intrusion

➤ Aquifer geometry effects on seawater intrusion depend on the aquifer width and distance from the circle center to the inner arc

1. **Introduction**

Islands are extensively distributed throughout the world's oceans. Unfortunately, their groundwater resources are impacted by sea-level rise and increased demands. According to a recent estimate, there are approximately 65 million people living in oceanic islands where groundwater may be the only source of freshwater (Thomas et al., 2020). Fresh groundwater stored on oceanic islands is mainly from precipitation (usually in the form of a freshwater lens) and its availability varies due to different factors, e.g., island topography, rainfall patterns, tides, episodic storms and human activities (White & Falkland, 2010; Storlazzi et al., 2018). Seawater intrusion is thus an important issue due to its deleterious effect on oceanic island freshwater storage (e.g., Werner et al., 2017; Lu et al., 2019; Memari et al., 2020).

In contrast to coastal aquifers where seawater intrudes into freshwater from one direction only, seawater intrusion occurs from four directions for narrow strip islands and from all directions for circular islands. Over the past few decades, seawater intrusion in oceanic islands has been extensively investigated in field observations (e.g., Röper et al., 2013; Post et al., 2019), laboratory experiments (e.g., Stoeckl et al., 2015; Bedekar et al., 2019; Memari et al., 2020), numerical simulations (e.g., Lam, 1974; Gingerich et al., 2017; Liu & Tokunaga, 2019) and analytical solutions (e.g., Fetter, 1972; Ketabchi et al., 2014; Lu et al., 2019). Among these, analytical solutions are effective tools to assess the extent of seawater intrusion (i.e., the location of the freshwater-seawater interface), although they cannot incorporate complex factors (e.g., dispersive mixing and transient oceanic dynamics) (Werner et al., 2013). The advantages of analytical solutions are that they are computationally efficient, can

be used as test cases for numerical models, and can reveal the explicit relationships between parameters that influence seawater intrusion (e.g., Fetter, 1972; Ketabchi et al., 2014; Liu et al., 2014; Lu et al., 2019;).

Based on the Dupuit-Forchheimer approximation (i.e., ignoring vertical flow) and the Ghijben-Herzberg equation (Drabbe & Badon Ghijben, 1889, English translation given by Post (2018); Herzberg, 1901), Fetter (1972) presented analytical solutions describing the freshwater-seawater interface location and watertable elevation in a circular island. Bailey et al. (2010) further compared these single-layered analytical solutions with field measurements, indicating that the analytical solutions perform well in estimating the freshwater-seawater interface location and watertable elevation. Fetter's solutions formed the foundation for many subsequent analytical studies on seawater intrusion in island aquifers. Again, for a single layer, Chesnaux and Allen (2008) and Greskowiak et al. (2013) developed analytical solutions to predict the steady-state groundwater age distribution in freshwater lenses. In addition, using single-layered analytical solutions, Morgan and Werner (2014) proposed vulnerability indicators of freshwater lenses under sea-level rise and recharge change.

Since aquifers are usually heterogeneous, the single-layer analytical solutions were subsequently extended to two-layered island aquifers. Vacher (1988) derived solutions for the freshwater-seawater interface location and watertable elevation for infinite-strip islands composed of different layers. Dose et al. (2014) conducted laboratory experiments to validate and confirm the reliability of analytical solutions proposed by Fetter (1972) and Vacher (1988). Ketabchi et al. (2014) extended Fetter's analytical solutions to calculate the

freshwater-seawater interface location and watertable elevation in two-layered circular islands subject to sea-level rise. Their results indicated that land-surface inundation caused by sea-level rise has a considerable impact on fresh groundwater lenses. Recently, Lu et al. (2019) derived analytical solutions for the freshwater-seawater interface location and watertable elevation for both strip and circular islands with two adjacent layers, i.e., a less permeable slice along the shoreline of an island, and a more permeable zone inland.

All the abovementioned analytical solutions apply to either strip or circular islands. According to the classification of sand dunes developed by Stuyfzand (1993; 2017), there are different island layouts that should be considered, e.g., where the shape of the island is an annulus segment, instead of a strip or circular disk (Figure 1). Annulus segment-shaped islands are found in various atolls (i.e., circular chains of islands surrounding a central lagoon) as found in the Pacific and Indian Oceans (Werner et al., 2017; Duvat, 2019). Nevertheless, analytical solutions of seawater intrusion are not yet available for annulus segment aquifers (ASAs). In general, ASAs are conceptually treated as a 2D cross section, similar to strip islands (e.g., Ayers & Vacher, 1986; Underwood et al., 1992; Bailey et al., 2009; Werner et al., 2017). Evidently, topography plays an important role in groundwater flow and hence seawater intrusion (e.g., Zhang et al., 2016; Liu & Tokunaga, 2019). It remains unclear whether analytical solutions of seawater intrusion for strip islands are appropriate for ASAs. It is moreover additionally unclear how island geometry affects the freshwater-seawater interface location and watertable elevation of ASAs.

In this study, analytical solutions are derived for steady-state seawater intrusion for ASAs,

with a focus on the freshwater-seawater interface location and its corresponding watertable

elevation. After comparing their predictions with experimental data (Memari et al., 2020), the

analytical solutions are employed to investigate the effects of aquifer geometry on the

freshwater-seawater interface location and watertable elevation in ASAs.

2. Conceptual Model

Figure 2 shows the conceptual model of an ASA (a slice of an atoll island). The plan

view of the model domain is represented as a sector (*EFGH*) with an angle θ (Figure 2a).

Radial flow only is considered. The sea (*EF*) and lagoon (*HG*) boundaries are located at $L +$

L_0 [L] and L_0 [L] from the circle center, respectively. Since the longitudinal length is usually

much longer than the lateral length for an atoll island (Werner et al., 2017), seawater intrusion

from the lateral sides (*EH* and *FG*, Figure 2a) is negligible in comparison to the longitudinal

side, especially for the middle portion of an ASA. Therefore, *EH* and *FG* are treated as lateral

no-flow boundaries. Note that treating the lateral sides as no-flow boundaries is often used in

studies of freshwater lenses on atoll islands (e.g., Ayers & Vacher, 1986; Underwood et al.,

1992; Bailey et al., 2009; Werner et al., 2017). The side view of the model domain is

conceptualized as a rectangle (*ABCD*) along the radial direction with dimensions of L [L]

(width) × d [L] (height) (Figure 2b, c). *AD* is the impermeable base while *BC* is the land

surface through which aquifer recharge flows.

Both the sea and lagoon water levels are set to H_s [L], which results in an internal no-

flow boundary (water divide, where the slope of the watertable is zero) between the sea and

lagoon (location of the *z*-axis in Figure 2b,c). The segment between the sea and the internal

no-flow boundary is referred to as Unit 1, whereas the segment between the internal no-flow

and lagoon boundaries is referred to as Unit 2 (Figure 2). The widths of Units 1 and 2 are l_1

[L] and l_2 [L], respectively. In addition, the flow is asymmetrical in Units 1 and 2, with

divergent flow (the aquifer width w [L] increases along the flow direction) in Unit 1 and

convergent flow (w decreases along the flow direction) in Unit 2.

The x-z coordinate origin is placed at the intersection of the internal no-flow boundary

and impermeable base, with the x-axis pointing to the circle center and the z-axis pointing

vertically upward. Further, ϕ [L] is the watertable height, h [L] is the vertical distance

between the watertable and the interface, h_s [L] is the vertical distance between the sea level

and the interface, and $h_c = H_s - h_s$ [L] is the vertical distance from the impermeable base to

the interface for given x (Figure 2b,c). Constant recharge into the saturated zone, N [LT^{-1}], is

assumed. There are two possibilities for the interface tip (i.e., the location where the

freshwater-seawater interface connects to the z-axis or the bottom boundary): above the

aquifer bed (Figure 2b) or on the aquifer bed (Figure 2c). The x-coordinates of the interface

tip in Units 1 and 2 are denoted as x_{t1} [L] and x_{t2} [L], respectively (Figure 2c). Note that x_{t1} =

x_{t2} = 0 when the interface tip is above the aquifer bed, as in Figure 2b.

Consistent with previous studies (e.g., Ketabchi et al., 2014; Lu et al., 2016; 2019), the

following assumptions are made: (1) steady-state flow, (2) sharp freshwater-seawater

interface, (3) homogeneous and isotropic aquifer, (4) negligible unsaturated flow, (5) recharge

is less than the saturated hydraulic conductivity (else overland flow will appear following

ponding), and (6) vertical flow in the saturated zone is negligible (Dupuit-Forchheimer

approximation).

3. Analytical Solutions

Groundwater flow in an ASA (Figure 2) can be described as (Paniconi et al., 2003; Troch

et al., 2003),

$$-\frac{\partial}{\partial x}(wq) + Nw = \frac{\partial S}{\partial t} \tag{1}$$

where q [L^{2}T^{-1}] is the Darcy flux per unit length along the aquifer, x [L] represents the

distance from the circle center to the arc, S [L^2] is the total water storage per unit distance

along the aquifer, and t [T] is time. Equation (1) is the so-called the hillslope-storage

Boussinesq equation and was first proposed by Troch et al. (2003). For a given radial distance

x, this equation assumes that the velocity is the same everywhere on the arc (w). Based on this

assumption, the 3D flow problem can be simplified to 1D, making it possible to consider

geometry effects analytically. Paniconi et al. (2003) validated equation (1) by comparing it

with a 3D Richards' equation model and found that predictions of equation (1) matched well

those of the 3D model for nine different geometries. Subsequently, equation (1) was used to

for further analyses (Hilbert et al., 2005, 2007; Hazenberg et al., 2015, 2016; Kong et al.,

2016; Luo et al., 2018). At steady state, equation (1) reduces to,

$$-\frac{\partial}{\partial x}(wq) + Nw = 0 \tag{2}$$

According to Darcy's law and the Dupuit-Forchheimer approximation, the freshwater

flux in the aquifer segment between the seaward boundary and interface tip can be calculated

as (ϕ is independent of z),

176
$$q = -\int_{h_c}^{\phi} K_s \frac{d\phi}{dx} dz = -K_s \left(\phi - h_c\right) \frac{d\phi}{dx} \tag{3}$$

177 where K_s [LT^{-1}] is the saturated hydraulic conductivity.

178 **3.1. Interface Tip above the Aquifer Bed**

179 We first consider the situation where the interface tip is above the aquifer bed (Figure

180 2b). In Unit 1 where $w = \theta\left(L_0 + l_2 - x\right)$, substituting equation (3) into equation (2) and then

181 integrating gives,

182
$$-\frac{1}{2}\left[\left(L_0 + l_2 - x\right)^2 - \left(L_0 + l_2\right)^2\right] N = -\left(L_0 + l_2 - x\right) K_s \left(\phi - h_c\right) \frac{d\phi}{dx} \tag{4}$$

183 According to the Ghijben-Herzberg equation, the vertical thickness of the freshwater zone (h)

184 in the interface zone is given by,

185
$$h = \phi - h_c = \left(1 + \alpha\right)\left(\phi - H_s\right) \tag{5}$$

186 where $\alpha = \rho_f / \left(\rho_s - \rho_f\right)$ is the dimensionless density difference, and ρ_f [ML^{-3}] and ρ_s

187 [ML^{-3}] are the freshwater and seawater densities, respectively. Substitution of equation (5)

188 into equation (4) yields,

189
$$-\frac{1}{2}\left[\left(L_0 + l_2 - x\right)^2 - \left(L_0 + l_2\right)^2\right] N = -K_s \left(L_0 + l_2 - x\right)\left(1 + \alpha\right)\left(\phi - H_s\right) \frac{d\phi}{dx} \tag{6}$$

190 Rearranging equation (6) produces,

191
$$-\frac{\left(L_0 + l_2 - x\right) N}{2} + \frac{N\left(L_0 + l_2\right)^2}{2\left(L_0 + l_2 - x\right)} = -K_s \left(1 + \alpha\right)\left(\phi - H_s\right) \frac{d\phi}{dx} \tag{7}$$

192 Integrating equation (7) leads to,

193
$$-\frac{\left(L_0 + l_2\right)^2 N}{2} \ln\left(L_0 + l_2 - x\right) - \frac{1}{2}\left(L_0 + l_2\right) Nx + \frac{1}{4} Nx^2 + C_1 = -K_s \left(1 + \alpha\right) \frac{\left(\phi - H_s\right)^2}{2} \tag{8}$$

194 where C_1 is the integration constant that is determined by the sea boundary condition (i.e.,

195 $x = -l_1$, $\phi = H_s$),

$$C_1 = \frac{(L_0 + l_2)^2 N}{2} \ln(L_0 + l_2 + l_1) - \frac{1}{2}(L_0 + l_2)l_1 N - \frac{1}{4}l_1^2 N \tag{9}$$

The relation between h_s and ϕ is given by,

$$h_s = \alpha(\phi - H_s) \tag{10}$$

Combining equation (8) with equation (10) and eliminating ϕ yields,

$$-\frac{(L_0 + l_2)^2 N}{2} \ln(L_0 + l_2 - x) - \frac{1}{2}(L_0 + l_2)Nx + \frac{1}{4}Nx^2 + C_1 = -K_s(1+\alpha)\frac{h_s^2}{2\alpha^2} \tag{11}$$

Equation (11) gives the freshwater-seawater interface location in Unit 1 once l_1 and l_2 are

determined.

Equation (8) applies to Unit 2 by replacing C_1 with C_2,

$$-\frac{(L_0 + l_2)^2 N}{2} \ln(L_0 + l_2 - x) - \frac{1}{2}(L_0 + l_2)Nx + \frac{1}{4}Nx^2 + C_2 = -K_s(1+\alpha)\frac{(\phi - H_s)^2}{2} \tag{12}$$

where C_2 is chosen to satisfy the lagoon boundary condition ($x = l_2$, $\phi = H_s$),

$$C_2 = \frac{(L_0 + l_2)^2 N}{2} \ln(L_0) + \frac{1}{2}(L_0 + l_2)l_2 N - \frac{1}{4}l_2^2 N \tag{13}$$

Combining equations (10) and (12) and eliminating ϕ leads to,

$$-\frac{(L_0 + l_2)^2 N}{2} \ln(L_0 + l_2 - x) - \frac{1}{2}(L_0 + l_2)Nx + \frac{1}{4}Nx^2 + C_2 = -K_s(1+\alpha)\frac{h_s^2}{2\alpha^2} \tag{14}$$

Equation (14) gives the freshwater-seawater interface location in Unit 2 once l_2 is

determined. Since the sea level and lagoon water level are the same, an internal no-flow

boundary exists between the sea and lagoon, i.e.,

$$x = 0, \ (h_s)_{unit1} = (h_s)_{unit2} \tag{15}$$

where $(h_s)_{unit1}$ and $(h_s)_{unit2}$ represent h_s in Units 1 and 2, respectively.

Combining equations (11), (14) and (15) leads to expressions for l_1 and l_2,

$$l_1 = L + L_0 - \sqrt{\frac{2LL_0 + L^2}{2\ln(L+L_0) - 2\ln(L_0)}} \qquad (16)$$

$$l_2 = \sqrt{\frac{2LL_0 + L^2}{2\ln(L+L_0) - 2\ln(L_0)}} - L_0 \qquad (17)$$

As indicated by equations (16) and (17), the internal no-flow boundary between the sea and

lagoon only depends on L and L_0. For known l_1 and l_2, equations (11) and (14) can be

employed to predict the freshwater-seawater interface location in Units 1 and 2, respectively.

Once the interface location is determined, h and ϕ are given by,

$$h = \frac{1+\alpha}{\alpha} h_s \qquad (18)$$

$$\phi = \frac{h_s}{\alpha} + H_s \qquad (19)$$

3.2. Interface Tip on the Aquifer Bed

When the interface tip is on the aquifer bed, the location of the internal no-flow

boundary remains the same as for the interface tip above the aquifer bed. The freshwater-

seawater interface for Units 1 and 2 can be determined by equations (11) and (14),

respectively. Then, from equation (18), h at the aquifer segment between the sea boundary and

the interface tip is determined. To calculate h for the aquifer segment between the interface tip

and the internal no-flow boundary, the x-coordinate of the interface tip is found. At the

interface tip of Unit 1 ($x = x_{t1}$),

$$h_s = H_s \qquad (20)$$

$$\phi = \frac{1+\alpha}{\alpha} H_s \qquad (21)$$

With equations (11) and (21), x_{t1} is given by,

$$-\frac{(L_0 + l_2)^2 N}{2} \ln(L_0 + l_2 - x_{t1}) - \frac{1}{2}(L_0 + l_2) N x_{t1} + \frac{1}{4} N x_{t1}^2 = -C_1 - K_s(1+\alpha)\frac{H_s^2}{2\alpha^2} \qquad (22)$$

Let,

$$a = \frac{1}{4}N \tag{23a}$$

$$b = -\frac{1}{2}(L_0 + l_2)N \tag{23b}$$

$$c = -\frac{(L_0 + l_2)^2 N}{2} \tag{23c}$$

and

$$m = -C_1 - K_s(1+\alpha)\frac{H_s^2}{2\alpha^2} \tag{23d}$$

then equation (22) becomes,

$$ax_{t1}^2 + bx_{t1} + c\ln(L_0 + l_2 - x_{t1}) = m \tag{24}$$

which is solved by a root-finding method.

The freshwater discharge for the aquifer segment between the interface tip and the

internal no-flow boundary is calculated as,

$$-\frac{1}{2}\left[(L_0 + l_2 - x)^2 - (L_0 + l_2)^2\right]N = -(L_0 + l_2 - x)K_s\phi\frac{d\phi}{dx} \tag{25}$$

Repeating the steps from equations (4) to (8) gives,

$$-\frac{(L_0 + l_2)^2 N}{2}\ln(L_0 + l_2 - x) - \frac{1}{2}(L_0 + l_2)Nx + \frac{1}{4}Nx^2 + C_3 = -\frac{K_s}{2}\phi^2 \tag{26}$$

where C_3 is determined by substituting equation (21) into equation (26). Then, equation (26)

can be adopted to calculate h for the segment between the interface tip and the internal no-

flow boundary where $h = \phi$.

Similarly, the x-coordinate of the interface tip in Unit 2 (x_{t2}) is obtained by substituting

equation (20) into equation (14). Then, the watertable (h) of the aquifer segment between the

interface tip and the internal no-flow boundary for Unit 2 is computed by repeating the steps

255 from equations (22) to (26).

4. Results and Discussion

4.1. Validation of the Analytical Solutions

258   The analytical solutions were validated by comparing their predictions with experimental

259 data compiled from Memari et al. (2020), who reported experiments carried out using a 15°

260 radial tank. The tank contained three distinct chambers: internal no-flow boundary condition,

261 porous medium and constant-head boundary condition (i.e., sea or lagoon). The internal no-

262 flow and seaward boundaries were respectively located at 10 cm and 55.5 cm from the circle

263 center, i.e., 45.5 cm from the internal no-flow boundary to the constant-head boundary along

264 the radial direction. Note that the experimental tank only corresponds to Unit 1 of the radial

265 aquifer with l_1 = 45.5 cm and l_2 = 0, so the analytical results were calculated using

266 equations (11) and (24). The thicknesses of the porous medium and sea level were 28 and 25

267 cm, respectively, with K_s = 1.23 × 10^{-2} m s^{-1}. The measured saltwater and freshwater densities

268 were respectively 1.015 and 0.999 g ml^{-1}, leading to $\alpha = 62$. Two different recharge events

269 with constant N, 2.46 × 10^{-4} and 1.08 × 10^{-4} m s^{-1}, were considered in the experiments.

270   Figure 3 shows the comparison between analytical and experimental results of the

271 freshwater-seawater interface for different recharge events. In general, the analytical solution

272 predicts the freshwater-seawater interface well for both recharge events, despite there being

273 some differences between the analytical results and the measurements, particularly in the zone

274 near the constant-head boundary (x = -45 cm). These deviations are likely due to assumptions

275 made in the analytical solution, i.e., (i) a sharp freshwater-seawater interface, (ii) ignoring the

effect of freshwater discharge, and (iii) neglecting the vertical flow (the Dupuit-Forchheimer approximation).

4.2. Effects of Aquifer Geometry on Seawater Intrusion

Previous studies showed that boundary conditions play a critical role in estimates of seawater intrusion (Werner & Simmons, 2009; Lu et al., 2016). Therefore, the internal no-flow boundary between the sea and lagoon was examined for various ASAs. As indicated by equations (16) and (17), this internal no-flow boundary depends only on L and L_0. The values of l_1 and l_2 calculated respectively from equations (16) and (17) are shown in Figure 4 for three typical values of L (500, 1000 and 2000 m) with L_0 varying from 10^2 to 10^6 m. In general, the internal no-flow boundary deviates from the middle of the ASA. When L_0 is less than 10^5 m, l_1 is larger than l_2 for the three different values of L, indicating an internal no-flow boundary closer to the lagoon boundary. For example, taking $L = 2000$ m and $L_0 = 100$ m leads to $l_1 = 1240$ m and $l_2 = 760$ m, with a deviation of 240 m (12% of 2000 m) from the middle of the ASA. When L_0 exceeds 10^5 m, however, the location of the internal no-flow boundary can be approximated as being at the middle of the ASA for all considered values of L. This is in contrast to strip and circular aquifers where the internal no-flow boundary is always in the middle of aquifers due to symmetry.

Since the internal no-flow boundary location between the sea and lagoon deviates from the middle of the ASA, we expect aquifer geometry to play a significant role in controlling seawater intrusion. As mentioned previously, ASAs can be convergent (Unit 1) or divergent aquifers (Unit 2) where the extent of seawater intrusion may be different. However, for strip

aquifers, both Units 1 and 2 are rectangular with the same extent of seawater intrusion.

Therefore, three geometries were compared in this study: convergent, rectangular and

divergent (Figure 5). These geometries have been widely examined in hillslope hydrology

regrading to the effects of aquifer geometry on runoff generation (Troch et al., 2003; Kong et

al., 2016; Luo et al., 2018). To present the results more conveniently, we replaced the x-z

coordinate origin at the intersection of the constant-head boundary (sea or lagoon) and the

impermeable base, with the x-axis pointing horizontally to the internal no-flow boundary and

the z-axis vertically upward (Figure 5). In addition, the distance between the constant-head

boundary and the internal no-flow boundary (aquifer width) is denoted as L^* (Figure 5) while

the other parameters remain the same.

Following previous studies (e.g., Lu et al., 2016; 2019), different cases were selected to

show the effects of aquifer geometry on seawater intrusion (Cases 1 and 2 in Table 1).

According to Werner et al. (2017), the width of atoll islands generally varies from 100 to 1500

m along the radial direction. In order to focus on the effects of aquifer geometry on seawater

intrusion, the same L^* and L_0 were assumed for the three aquifers, with L^* and L_0 equal to

1000 and 200 m, respectively. Note that L_0 is the distance from the circle center to the lagoon

boundary for convergent aquifers, whereas it represents the distance from the circle center to

internal no-flow boundary for divergent aquifers hereafter. The sand characteristics were the

same as in the experiments of Memari et al. (2020). Two recharge events were considered

(Cases 1 and 2, Table 1). The freshwater-seawater interface was calculated using the

analytical solutions for the three different aquifers. Note that the Appendix presents analytical

solutions for seawater intrusion in strip aquifers deduced from Lu et al. (2019).

Figure 6 shows the freshwater-seawater interface calculated for Cases 1 and 2. As can be seen, the extent of seawater intrusion is noticeably different for the three aquifer geometries. For high recharge (1×10^{-6} m s^{-1}), the interface tip is located at around 500 m for the divergent aquifer, which is about twice the value of the rectangular aquifer and six times the value for the convergent aquifer (Figure 6a). When the recharge decreases to 3×10^{-7} m s^{-1}, the interface tip moves further landward for the three aquifers as expected, but the difference between results is still great (Figure 6b). The interface tip is displaced above the aquifer bed for both the rectangular and divergent aquifers, while it remains on the aquifer bed for the convergent aquifer. Regardless of the recharge rate, the most landward freshwater-seawater interface occurs in the divergent aquifer and vice versa for the convergent aquifer. This underlines that aquifer geometry plays a major role in controlling seawater intrusion and hence it is necessary to account for aquifer geometry in analyses of seawater intrusion.

4.3. Sensitivity Analysis

A sensitivity analysis was conducted to investigate to what extent aquifer geometry affects seawater intrusion. Since we focus on the effects of aquifer geometry on the locations of the freshwater-seawater interface and watertable, values of L_0 and L^* were varied, with other parameters kept constant. When conducting the sensitivity analysis of L_0, L^* was fixed at 1000 m, which is a typical value for ASAs (Werner et al., 2017). Figure 7 shows the sensitivity of the locations of the freshwater-seawater interface and watertable to changes in L_0 (Case 3, Table 1). The freshwater-seawater interface and watertable elevation are

independent of L_0 for rectangular aquifers (Appendix). However, the freshwater-seawater interface and watertable elevation differ greatly when varying L_0 for both convergent and divergent aquifers, highlighting that L_0 plays an important role in affecting seawater intrusion. Specifically, as L_0 increases, the freshwater-seawater interface moves more landward (larger x/L^*, Figure 7a) and its corresponding watertable elevation decreases (Figure 7c) for convergent aquifers. In contrast, for divergent aquifers increasing L_0 moves the freshwater-seawater interface more seaward (smaller x/L^*, Figure 7b) and its corresponding watertable elevation increases (Figure 7d). For a given L_0, divergent aquifers have the largest extent of seawater intrusion and the lowest watertable elevation, and conversely for convergent aquifers (Figure 7).

Regardless of the freshwater-seawater interface and watertable elevation, the deviation between rectangular aquifers and divergent or convergent aquifers is significant when L_0 is less than 2000 m (Figure 7). For example, the x-coordinate of the interface tip ($z = 0$) is 262 m for the rectangular aquifer at $L_0 = 200$ m, whereas it is 78 (31% of that in the rectangular aquifer) and 500 m (191% of that in the rectangular aquifer) for the convergent and divergent aquifers, respectively. As L_0 increases, the deviation between the three aquifers decreases. When $L_0 = 2000$ m, the x-coordinate of the interface tip is 262, 209 (80% of that in the rectangular aquifer) and 318 m (121% of that in the rectangular aquifer) for the rectangular, convergent and divergent aquifers, respectively. As L_0 increases to 6000 m, the freshwater-seawater interface and watertable elevation of both convergent and divergent aquifers tend to those of rectangular aquifers, i.e., geometry effects decrease with increasing L_0. These results

highlight the critical role played by the shape of aquifers. As a result, ignoring the aquifer geometry may lead to an inappropriate management strategy for groundwater resources in atoll islands.

The sensitivity of the freshwater-seawater interface and watertable elevation to L^* was investigated by varying L^* from 600 to 1600 m while fixing L_0 to 200 m (Case 4, Table 1). As shown in Figure 8, contrary to the results for varying L_0, in this case the freshwater-seawater interface and watertable elevation in all three topographies are related to L^*. Again, the extent of seawater intrusion is greatest in divergent aquifers and least in convergent aquifers for given L^*. When L^* increases, the freshwater-seawater interface moves seaward and the watertable elevation increases, regardless of aquifer geometry, i.e., the seawater intrusion decreases (Figures 8a-c). This is because the total freshwater flux increases with increasing L^*, leading to a higher hydraulic gradient and hence less seawater intrusion (Figures 8d-f). Moreover, an increase in L^* reduces the differences in the seawater intrusion distance among the three geometries, i.e., the effects of aquifer geometry on seawater intrusion are more significant at small L^*. However, even at the maximum L^* considered (1600 m), the deviation between three aquifers remains significant: The x-coordinate of the interface tip is about 148 m for the rectangular aquifer, whereas it is about 32 (22% of that in the rectangular aquifer) and 278 m (188% of that in the rectangular aquifer) for the convergent and divergent aquifers, respectively. Both L_0 and L^* can greatly impact seawater intrusion estimates for divergent and convergent aquifers, highlighting the necessity to include geometry effects in analytical solutions of seawater intrusion.

5. Conclusions

Based on the Ghijben-Herzberg and hillslope-storage Boussinesq equations, we derived analytical solutions of steady-state seawater intrusion for ASAs, with a focus on the freshwater-seawater interface and its corresponding watertable elevation as affected by recharge. After comparing with experimental data of Memari et al. (2020), the analytical solutions were employed to examine the effects of aquifer geometry on seawater intrusion in island aquifers. Three different shapes of island aquifer were compared: convergent, rectangular and divergent. The results lead to the following conclusions:

- The presented analytical solutions perform well in predicting the experimental freshwater-seawater interface, suggesting that these analytical solutions can predict seawater intrusion reasonably in different aquifer geometries.

- Island geometry plays a significant role in affecting the freshwater-seawater interface and watertable elevation. Other factors being equal, the extent of seawater intrusion is greatest in divergent aquifers, and conversely least in convergent aquifers. In contrast, the watertable elevation is lowest in divergent aquifers and highest in convergent aquifers.

- The effects of aquifer geometry on seawater intrusion are dependent on the aquifer width and distance from the circle center to the internal no-flow boundary (Figures 7 and 8). A larger aquifer width and distance from the circle center to the inner arc (the lagoon boundary for convergent aquifers while the internal no-flow boundary for divergent aquifers) weakens the role played by aquifer geometry and hence lead to a smaller deviation of the extent of seawater intrusion between the three topographies.

402   Real island aquifers are expected to exhibit more complexity than considered here, e.g.,

403   that will have more complex shapes and are subjected to transient flow conditions caused by

404   tides, waves and groundwater pumping (Mantoglou et al. 2003; Pool & Carrera., 2011;

405   Werner et al., 2013). In addition, since the experimental scale of Memari et al. (2020) is

406   necessarily small, future experiments and field data are needed to further validate and

407   facilitate the analytical solutions. Despite this, the new analytical solutions, validated against

408   experiments, can be used as a tool for rapid estimation of seawater intrusion in ASAs once

409   known island geometry and corresponding soil properties are given.

 Appendix: Analytical Solutions for Rectangular Aquifers

For rectangular aquifers, the seawater intrusion in Unit 1 is identical to that in Unit 2

because of symmetry. With the interface tip on the aquifer bed, analytical solutions for the

freshwater-seawater interface (h_s), watertable elevation (h), and x-coordinate of the interface

tip in Unit 2 (x_{t2}) can be respectively written as (Lu et al., 2019),

$$h_s = \alpha \sqrt{\frac{N}{(1+\alpha)K_s}\left(\frac{L^2}{4} - x^2\right)} \tag{A1}$$

$$h = \begin{cases} \sqrt{\dfrac{N}{K_s}\left(x_{t2}^2 - x^2\right) + \left(\dfrac{H_s}{\alpha} + H_s\right)} & 0 \le x \le x_{t2} \\[4mm] \sqrt{\dfrac{N}{(1+\alpha)K_s}\left(\dfrac{L^2}{4} - x^2\right)} + H_s & x_{t2} < x \le \dfrac{L}{2} \end{cases} \tag{A2}$$

$$x_{t2} = \sqrt{\frac{L^2}{4} - \frac{(1+\alpha)K_s}{N}\left(\frac{H_s^2}{\alpha^2}\right)} \tag{A3}$$

When the interface tip is above the aquifer bed, the analytical solution for the freshwater-

seawater interface location and watertable elevation in Unit 2 are the same as equations (A1)

and (A2), respectively.

Code/Data availability

Experimental data used in this study are compiled from Memari et al. (2020).

Author contributions

423

424   All authors contributed to the design of the research. ZL carried out data collation,

425   developed the analytical solutions and prepared the manuscript with contributions from all

426   co-authors. All authors contributed to the interpretation of the results and provided feedback.

Competing interests

The authors declare that they have no conflicts of interest.

Acknowledgments

This research was supported by the National Key R&D Program of China (2019YFC0409004) and the National Natural Science Foundation of China (51979095 and 41807178). ZL acknowledges EPFL for financial support and JK acknowledges the Qing Lan Project of Jiangsu Province (2020).

References

Ayers, J. F., & Vacher, H. L. (1986). Hydrogeology of an atoll island: A conceptual model from detailed study of a Micronesian example. *Groundwater*, *24*(2), 185-198. https://doi.org/10.1111/j.1745-6584.1986.tb00994.x

Bailey, R. T., Jenson, J. W., & Olsen, A. E. (2010). Estimating the ground water resources of atoll islands. *Water*, *2*(1), 1-27. https://doi.org/10.3390/w2010001

Bailey, R. T., Jenson, J. W., & Olsen, A. E. (2009). Numerical modeling of atoll island hydrogeology. *Groundwater*, *47*(2), 184-196. https://doi.org/10.1111/j.1745-6584.2008.00520.x

Bedekar, V. S., Memari, S. S., & Clement, T. P. (2019). Investigation of transient freshwater storage in island aquifers. *Journal of Contaminant Hydrology*, *221*, 98-107. https://doi.org/10.1016/j.jconhyd.2019.02.004

Chesnaux, R., & Allen, D. M. (2008). Groundwater travel times for unconfined island aquifers bounded by freshwater or seawater. *Hydrogeology Journal*, *16*(3), 437-445. https://doi.org/10.1007/s10040-007-0241-6

Dose, E. J., Stoeckl, L., Houben, G. J., Vacher, H. L., Vassolo, S., Dietrich, J., & Himmelsbach, T. (2014). Experiments and modeling of freshwater lenses in layered aquifers: Steady state interface geometry. *Journal of Hydrology*, *509*, 621-630. https://doi.org/10.1016/j.jhydrol.2013.10.010

Drabbe J. & Badon Ghijben, W. (1889). *Nota in verband met de voorgenomen put boring nabij Amsterdam*. Tijdschrift van het Koninklijk Instituut van Ingenieurs. pp. 8-22,

Gravenhage, Netherlands.

Duvat, V. K. E. (2019). A global assessment of atoll island planform changes over the past

decades. *Wiley Interdisciplinary Reviews: Climate Change*, *10*(1), e557.

https://doi.org/10.1002/wcc.557

Fetter, C. W. (1972). Position of the saline water interface beneath oceanic islands. *Water

Resources Research*, *8*(5), 1307-1315. https://doi.org/10.1029/WR008i005p01307

Gingerich, S. B., Voss, C. I., & Johnson, A. G. (2017). Seawater-flooding events and impact

on freshwater lenses of low-lying islands: Controlling factors, basic management and

mitigation. *Journal of Hydrology*, *551*, 676-688.

https://doi.org/10.1016/j.jhydrol.2017.03.001

Greskowiak, J., Röper, T., & Post, V. E. (2013). Closed-form approximations for two-

dimensional groundwater age patterns in a fresh water lens. *Groundwater*, *51*(4), 629-

634. https://doi.org/10.1111/j.1745-6584.2012.00996.x

Hazenberg, P., Fang, Y., Broxton, P., Gochis, D., Niu, G. Y., Pelletier, J. D., Troch., P. A., &

Zeng, X. (2015). A hybrid-3D hillslope hydrological model for use in Earth system

models. *Water Resources Research*, *51*(10), 8218-8239.

https://doi.org/10.1002/2014WR016842

Hazenberg, P., Broxton, P., Gochis, D., Niu, G. Y., Pangle, L. A., Pelletier, J. D., Troch., P. A.,

& Zeng, X. (2016). Testing the hybrid-3-D hillslope hydrological model in a

controlled environment. *Water Resources Research*, *52*(2), 1089-1107.

https://doi.org/10.1002/2015WR018106

Herzberg, A. (1901). Die wasserversorgung einiger Nordseebäder. *Journal für*

Gasbeleuchtung und Wasserversorgung, *44*, 815-819, *45*, 842-844.

Hilberts, A. G. J., Troch, P. A., & Paniconi, C. (2005). Storage-dependent drainable porosity

for complex hillslopes. *Water Resources Research*, *41*(6), W06001.

https://doi.org/10.1029/2004WR003725

Hilberts, A. G., Troch, P. A., Paniconi, C., & Boll, J. (2007). Low-dimensional modeling of

hillslope subsurface flow: Relationship between rainfall, recharge, and unsaturated

storage dynamics. *Water Resources Research*, *43*(3), W03445.

https://doi.org/10.1029/2006WR004964

Ketabchi, H., Mahmoodzadeh, D., Ataie-Ashtiani, B., Werner, A. D., & Simmons, C. T.

(2014). Sea-level rise impact on fresh groundwater lenses in two-layer small islands.

Hydrological Processes, *28*(24), 5938-5953. https://doi.org/10.1002/hyp.10059

Kong, J., Shen, C., Luo, Z., Hua, G., & Zhao, H. (2016). Improvement of the hillslope-storage

Boussinesq model by considering lateral flow in the unsaturated zone. *Water*

Resources Research, *52*(4), 2965-2984. https://doi.org/10.1002/2015WR018054

Lam, R. K. (1974). Atoll permeability calculated from tidal diffusion. *Journal of Geophysical*

Research, *79*(21), 3073-3081. https://doi.org/10.1029/JC079i021p03073

Liu, J., & Tokunaga, T. (2019). Future risks of tsunami-induced seawater intrusion into

unconfined coastal aquifers: Insights from numerical simulations at Niijima Island,

Japan. *Water Resources Research*, *55*(12), 10082-10104.

https://doi.org/10.1029/2019WR025386

Liu, Y., X. Mao, J. Chen, and D. A. Barry. 2014. Influence of a coarse interlayer on seawater

intrusion and contaminant migration in coastal aquifers. *Hydrological Processes*, *28*(20),

5162-5175. https://dx.doi.org/10.1002/hyp.10002

Lu, C., Cao, H., Ma, J., Shi, W., Rathore, S. S., Wu, J., & Luo, J. (2019). A proof-of-concept

study of using a less permeable slice along the shoreline to increase fresh groundwater

storage of oceanic islands: Analytical and experimental validation. *Water Resources*

Research, *55*(8), 6450-6463. https://doi.org/10.1029/2018WR024529

Lu, C., Xin, P., Kong, J., Li, L., & Luo, J. (2016). Analytical solutions of seawater intrusion in

sloping confined and unconfined coastal aquifers. *Water Resources Research*, *52*(9),

6989-7004. https://doi.org/10.1002/2016WR019101

Luo, Z., Shen, C., Kong, J., Hua, G., Gao, X., Zhao, Z., Zhao, H., & Li, L. (2018). Effects of

unsaturated flow on hillslope recession characteristics. *Water Resources Research*,

54(3), 2037-2056. https://doi.org/10.1002/2017WR022257

Mantoglou, A. (2003). Pumping management of coastal aquifers using analytical models of

saltwater intrusion. *Water Resources Research*, *39*(12), 1335.

https://doi.org/10.1029/2002WR001891

Memari, S. S., Bedekar, V. S., & Clement, T. P. (2020). Laboratory and numerical

investigation of saltwater intrusion processes in a circular island aquifer. *Water*

Resources Research, *56*(2), e2019WR025325. https://doi.org/10.1029/2019WR025325

Morgan, L. K., & Werner, A. D. (2014). Seawater intrusion vulnerability indicators for

freshwater lenses in strip islands. *Journal of Hydrology*, *508*, 322-327.

518   https://doi.org/10.1016/j.jhydrol.2013.11.002

519   Paniconi, C., Troch, P. A., Van Loon, E. E., & Hilberts, A. G. (2003). Hillslope-storage

520   Boussinesq model for subsurface flow and variable source areas along complex

521   hillslopes: 2. Intercomparison with a three-dimensional Richards equation model.

522   *Water Resources Research*, *39*(11), 1317. https://doi.org/10.1029/2002WR001730

523   Pool, M., & Carrera, J. (2011). A correction factor to account for mixing in Ghyben-Herzberg

524   and critical pumping rate approximations of seawater intrusion in coastal aquifers.

525   *Water Resources Research*, *47*(5), W05506. https://doi.org/10.1029/2010WR010256

526   Post, V. E. (2018). Annotated translation of "Nota in verband met de voorgenomen putboring

527   nabij Amsterdam [Note concerning the intended well drilling near Amsterdam]" by J.

528   Drabbe and W. Badon Ghijben (1889). *Hydrogeology Journal*, *26*(6), 1771-1788.

529   https://doi.org/10.1007/s10040-018-1797-z

530   Post, V. E. A., Houben, G. J., Stoeckl, L., & Sültenfuß, J. (2019). Behaviour of tritium and

531   tritiogenic helium in freshwater lens groundwater systems: Insights from Langeoog

532   Island, Germany. *Geofluids*, Volume *2019*, Article ID 1494326.

533   https://doi.org/10.1155/2019/1494326

534   Röper, T., Greskowiak, J., Freund, H., & Massmann, G. (2013). Freshwater lens formation

535   below juvenile dunes on a barrier island (Spiekeroog, Northwest Germany). *Estuarine,*

536   *Coastal and Shelf Science*, *121-122*, 40-50. https://doi.org/10.1016/j.ecss.2013.02.004

537   Stoeckl, L., Houben, G. J., & Dose, E. J. (2015). Experiments and modeling of flow processes

538   in freshwater lenses in layered island aquifers: Analysis of age stratification, travel

times and interface propagation. *Journal of Hydrology*, *529*, 159-168.

https://doi.org/10.1016/j.jhydrol.2015.07.019

Storlazzi, C. D., Gingerich, S. B., van Dongeren, A., Cheriton, O. M., Swarzenski, P. W.,

Quataert, E., Voss, C. I., Field, D. W., Annamalai, H., Piniak, G. A., & McCall, R.

(2018). Most atolls will be uninhabitable by the mid-21st century because of sea-level

rise exacerbating wave-driven flooding. *Science Advances*, *4*(4), eaap9741.

https://doi.org/10.1126/sciadv.aap9741

Strack, O. D. L. (1976). A single-potential solution for regional interface problems in coastal

aquifers. *Water Resources Research*, *12*(6), 1165-1174.

https://doi.org/10.1029/WR012i006p01165

Stuyfzand, P. J. (2017). Observations and analytical modeling of freshwater and rainwater

lenses in coastal dune systems. *Journal of Coastal Conservation*, *21*(5), 577-593.

https://doi.org/10.1007/s11852-016-0456-6

Stuyfzand, P. J. (1993). *Hydrochemistry and hydrology of the coastal dune area of the Western

Netherlands*. Ph.D. Thesis. Vrije University, Amsterdam, KIWA, ISBN 90-74741-01-

0. http://dare.ubvu.vu.nl/handle/1871/12716

Thomas, A., Baptiste, A., Martyr-Koller, R., Pringle, P., & Rhiney, K. (2020). Climate change

and small island developing states. *Annual Review of Environment and Resources*,

45(1), 1-27. https://doi.org/10.1146/annurev-environ-012320-083355

Troch, P. A., Paniconi, C., & Emiel van Loon, E. (2003). Hillslope-storage Boussinesq model

for subsurface flow and variable source areas along complex hillslopes: 1.

Formulation and characteristic response. *Water Resources Research*, *39*(11), 1316.

https://doi.org/10.1029/2002WR001728

Underwood, M. R., Peterson, F. L., & Voss, C. I. (1992). Groundwater lens dynamics of atoll

islands. *Water Resources Research*, *28*(11), 2889-2902.

https://doi.org/10.1029/92WR01723

Vacher, H. L. 1988. Dupuit-Ghyben-Herzberg analysis of strip-island lenses. *Geological*

Society of America Bulletin, *100*, 580-591. https://doi.org/10.1130/0016-

7606(1988)100<0580:DGHAOS>2.3.CO;2

Werner, A. D., Sharp, H. K., Galvis, S. C., Post, V. E., & Sinclair, P. (2017). Hydrogeology

and management of freshwater lenses on atoll islands: Review of current knowledge

and research needs. *Journal of Hydrology*, *551*, 819-844.

https://doi.org/10.1016/j.jhydrol.2017.02.047

Werner, A. D., Bakker, M., Post, V. E., Vandenbohede, A., Lu, C., Ataie-Ashtiani, B.,

Simmons, C. T., & Barry, D. A. (2013). Seawater intrusion processes, investigation

and management: Recent advances and future challenges. *Advances in Water*

Resources, *51*, 3-26. https://doi.org/10.1016/j.advwatres.2012.03.004

Werner, A. D., & Simmons, C. T. (2009). Impact of sea-level rise on sea water intrusion in

coastal aquifers. *Groundwater*, *47*(2), 197-204. https://doi.org/10.1111/j.1745-

6584.2008.00535.x

White, I., & Falkland, T. (2010). Management of freshwater lenses on small Pacific islands.

Hydrogeology Journal, *18*(1), 227-246. https://doi.org/10.1007/s10040-009-0525-0

581   Zhang, Y., Li, L., Erler, D. V., Santos, I., & Lockington, D. (2016). Effects of alongshore

582   morphology on groundwater flow and solute transport in a nearshore aquifer. *Water*

583   *Resources Research*, *52*(2), 990-1008. https://doi.org/10.1002/2015WR017420

584   **Table 1.** List of parameters use in different simulations.

	No.	L^* (m)	L_0 (m)	H_s (m)	d (m)	α (-)	K_s (m s^{-1})	N (m s^{-1})
	1	1000	200	38	45	40	1.23×10^{-2}	1×10^{-6}
	2	1000	200	38	45	40	1.23×10^{-2}	3×10^{-7}
Cases								
	3	1000	†	38	45	40	1.23×10^{-2}	1×10^{-6}
	4	†	200	38	45	40	1.23×10^{-2}	1×10^{-6}

585   †The parameter is varied: The range of L_0 is from 200 to 6000 m, whereas the range of L^* is

586   from 600 to 1600 m.

587

Figure 1. Island with an annulus segment in the Namu Atoll, Marshall Islands (© Google

589 Earth).

590
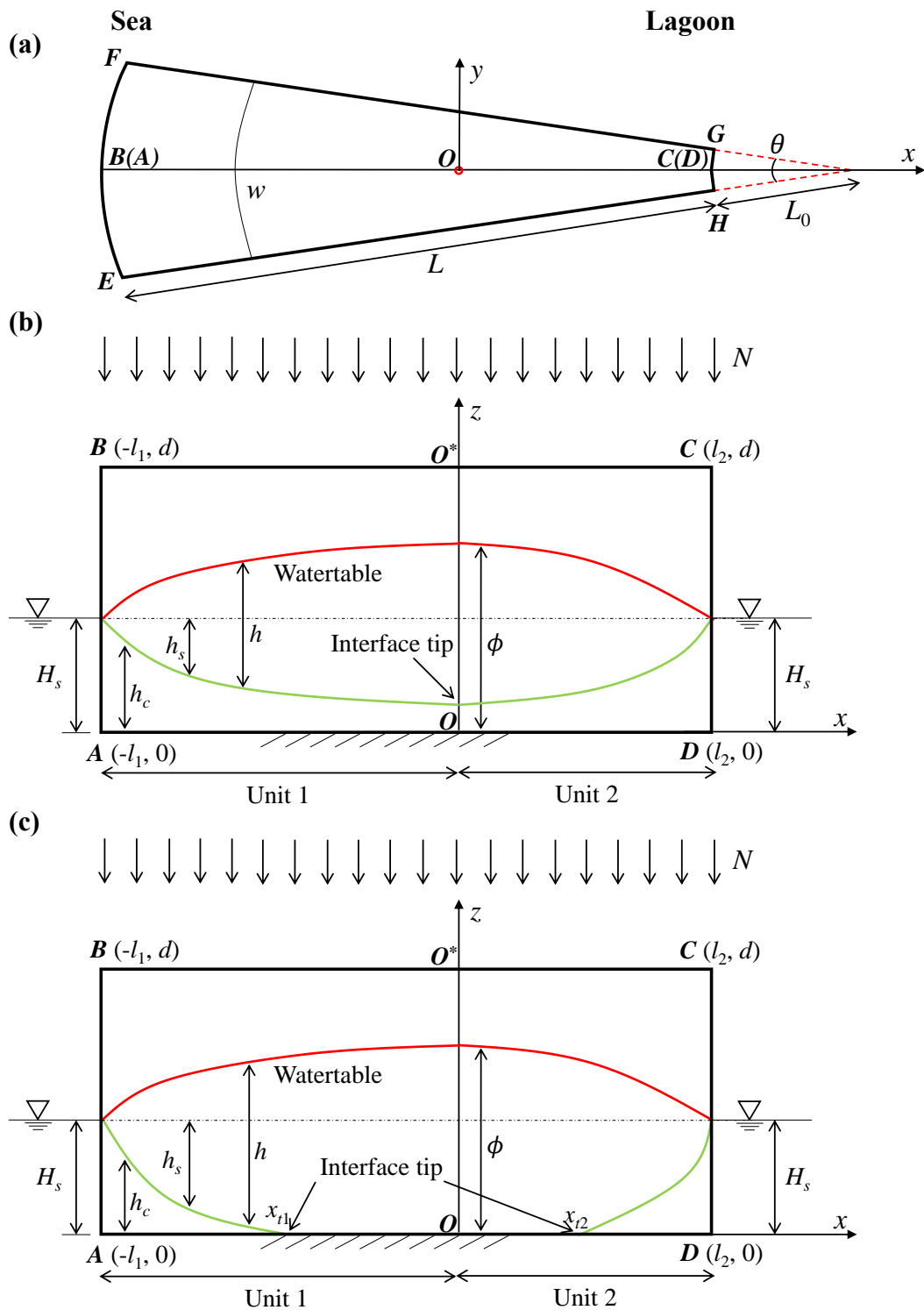
Figure 2. Conceptual model of an annulus segment aquifer (a slice of an atoll island). (a) Plan

view and (b, c) side view with the saltwater interface tip (b) above the aquifer bed (single

location) and (c) on the aquifer bed (two locations). In (a), the sea boundary is on *EF* and the

atoll lagoon boundary is on *HG*; In (b) and (c), *AD* is the impermeable base and OO^* is the

595   internal no-flow boundary.

596
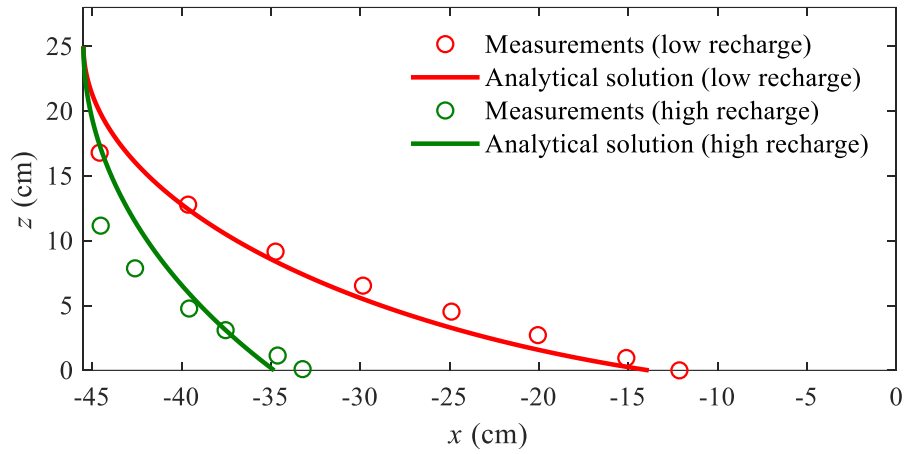
Figure 3. Comparison between analytical and experimental (data compiled from Memari et al., 2020) results for the freshwater-seawater interface location for different recharge events. Note that the left and right sides are the sea and internal no-flow boundaries, respectively.
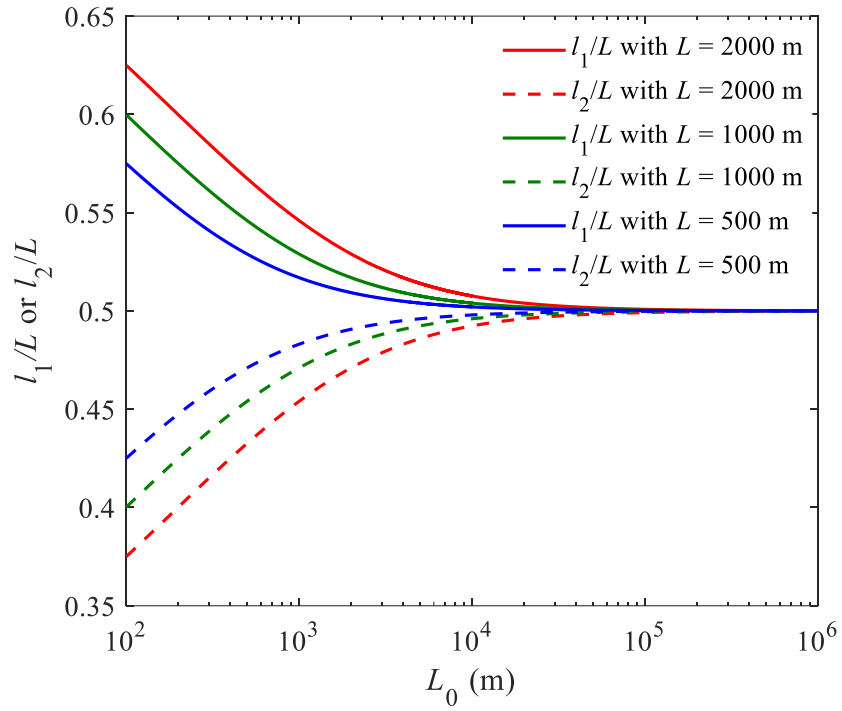
600

601   **Figure 4.** Widths of Unit 1 and Unit 2 versus L_0 for aquifers with different total width L.
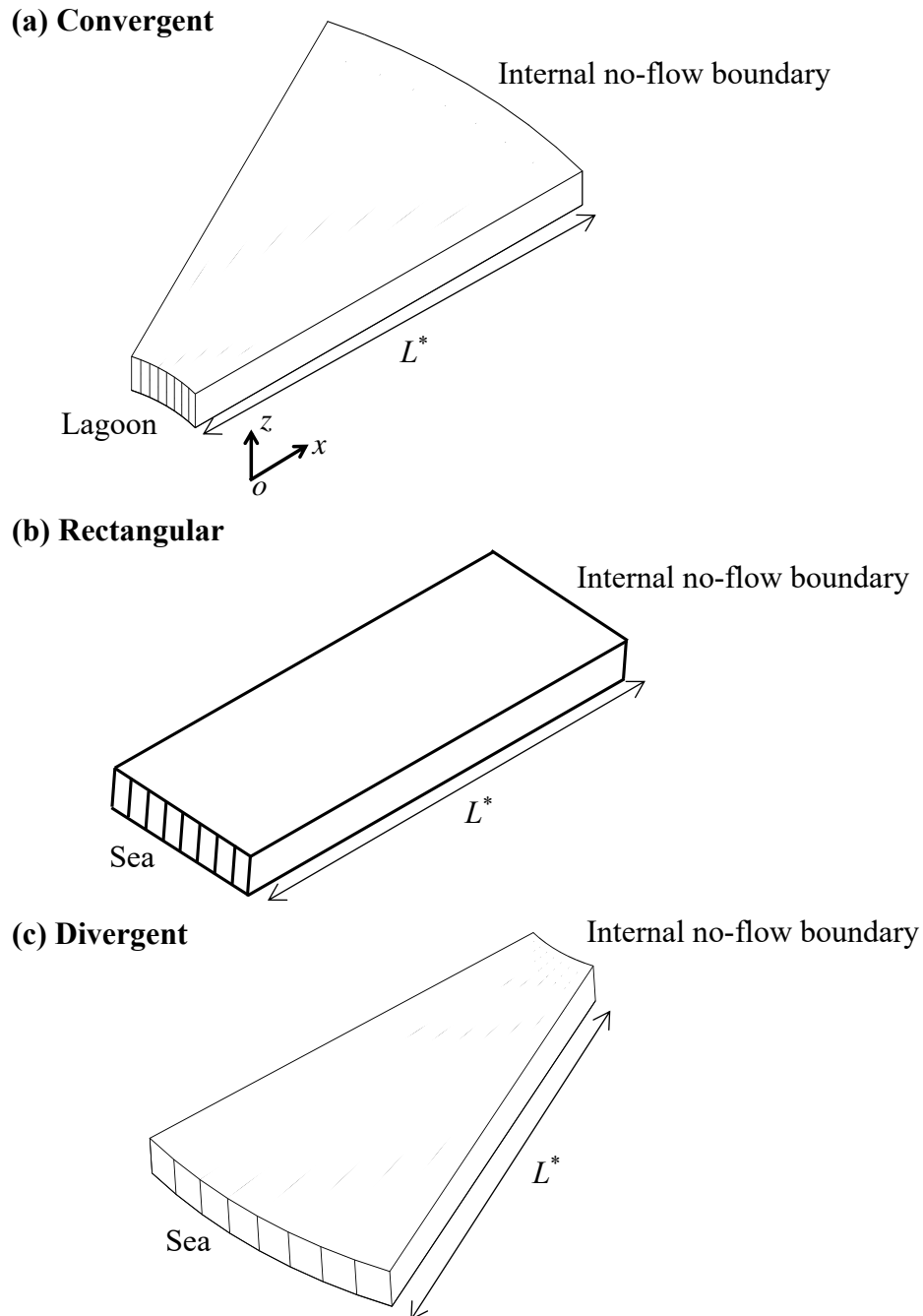
Figure 5. Three-dimensional view of (a) convergent (smaller side facing the lagoon), (b) rectangular and (c) divergent aquifers (larger side facing the sea) compared in this study. L^* represents the distance from the sea/lagoon to the internal no-flow boundary, i.e., l_1 or l_2 in Figure 2. The internal no-flow boundary corresponds to the z-axis in Figure 2.
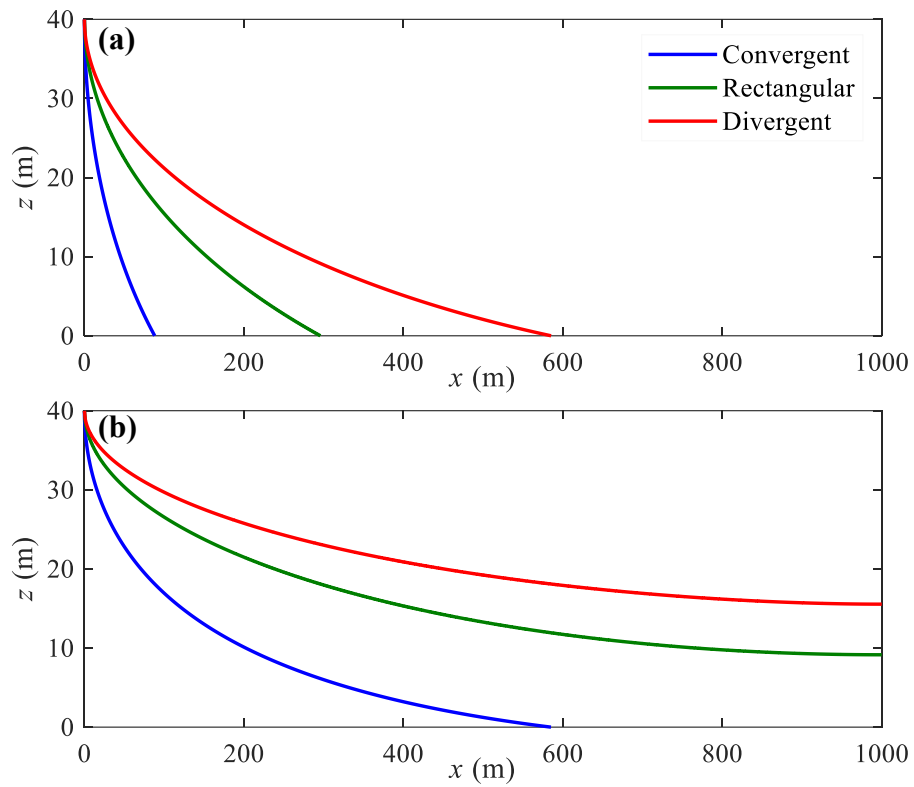
Figure 6. Freshwater-seawater interface predicted by analytical solutions for three different

aquifers with (a) high and (b) low recharge (Cases 1 and 2 in Table 1). Note that $x = 1000$ m is

the internal no-flow boundary in Figure 5.
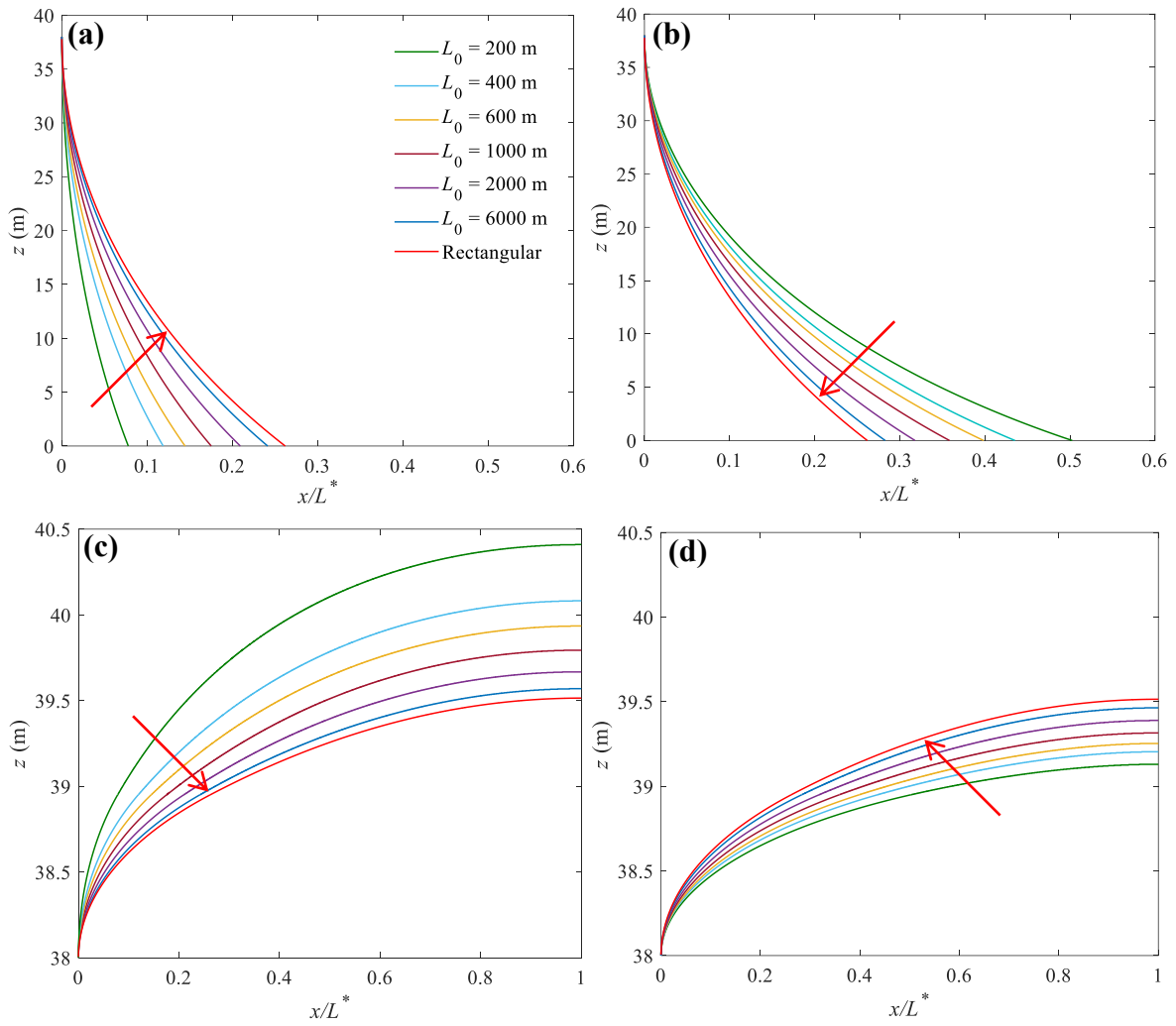
Figure 7. Sensitivity of (a, b) the locations of the freshwater-seawater interface and (c, d)

watertable to L_0 for convergent (left panel) and divergent (right panel) aquifers. The arrow in

each plot shows the direction of increasing L_0 (values given in (a), used to produce the

different curves). Note that predictions for rectangular aquifers are independent of L_0.
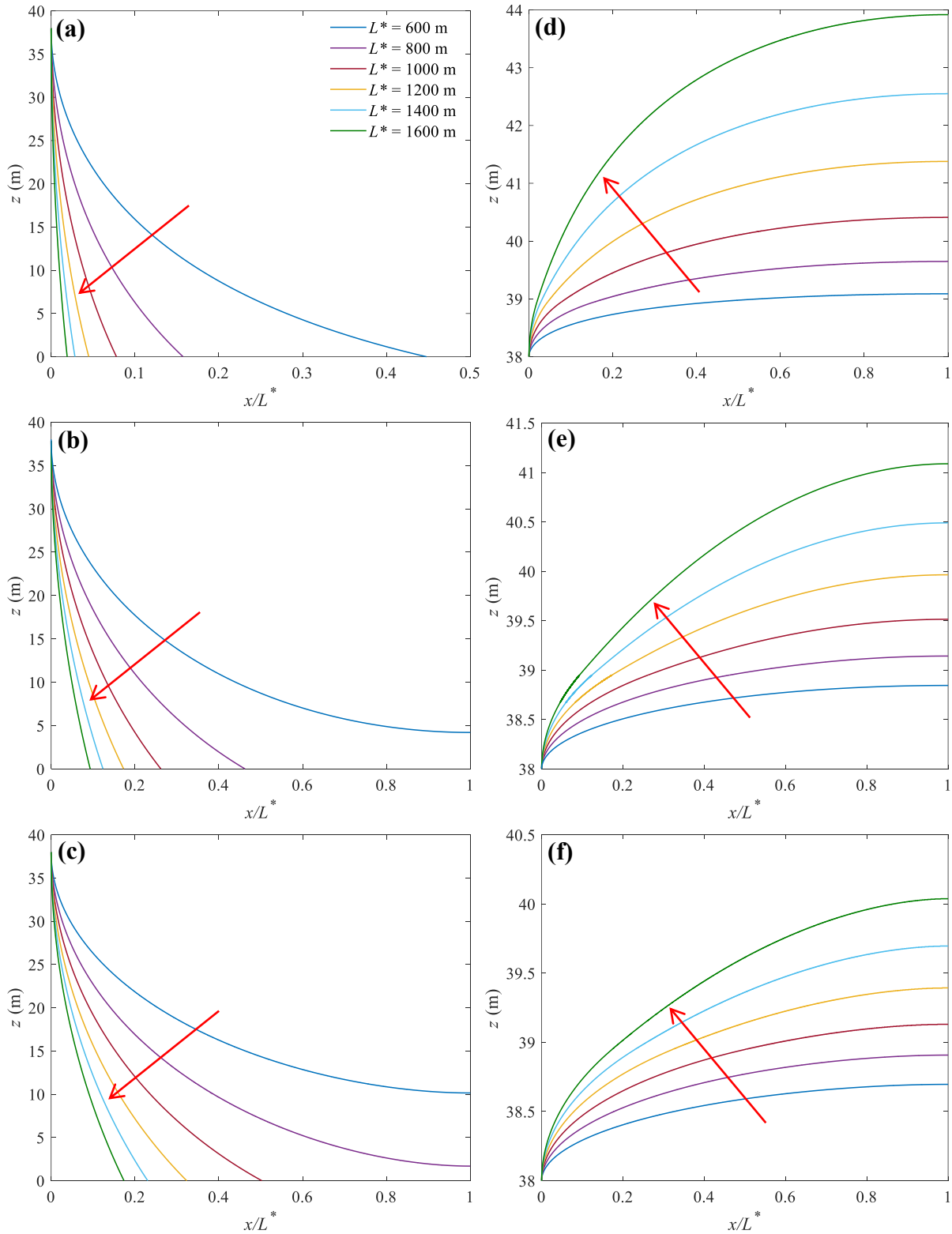
Figure 8. Sensitivity of (a-c) the locations of the freshwater-seawater interface and (d-f) watertable to L^* for convergent (a, d), rectangular (b, e) and divergent (c, f) aquifers. The arrow in each plot points to the increase of L^* values used to construct each curve (values

626   indicated in (a)).